

Pressure dependence of Kapitza resistance at gold/water and silicon/water interfaces

An Pham, Murat Barisik, and BoHung Kim

Citation: *The Journal of Chemical Physics* **139**, 244702 (2013); doi: 10.1063/1.4851395

View online: <http://dx.doi.org/10.1063/1.4851395>

View Table of Contents: <http://scitation.aip.org/content/aip/journal/jcp/139/24?ver=pdfcov>

Published by the [AIP Publishing](#)



Re-register for Table of Content Alerts

Create a profile.



Sign up today!



Pressure dependence of Kapitza resistance at gold/water and silicon/water interfaces

An Pham,¹ Murat Barisik,² and BoHung Kim^{1,a)}

¹*School of Mechanical Engineering, University of Ulsan, Daehak-ro 93, Namgu, Ulsan, South Korea*

²*Mechanical Engineering Department, Southern Methodist University, Dallas, Texas 75275, USA*

(Received 9 September 2013; accepted 5 December 2013; published online 26 December 2013)

We conducted non-equilibrium molecular dynamics simulations to investigate Kapitza length at solid/liquid interfaces under the effects of bulk liquid pressures. Gold and silicon were utilized as hydrophilic and hydrophobic solid walls with different wetting surface behaviors, while the number of confined liquid water molecules was adjusted to obtain different pressures inside the channels. The interactions of solid/liquid couples were reparameterized accurately by measuring the water contact angle of solid substrates. In this paper, we present a thorough analysis of the structure, normal stress, and temperature distribution of liquid water to elucidate thermal energy transport across interfaces. Our results demonstrate excellent agreement between the pressures of liquid water in nano-channels and published thermodynamics data. The pressures measured as normal stress components were characterized using a long cut-off distance reinforced by a long-range van der Waals tail correction term. To clarify the effects of bulk liquid pressures on water structure at hydrophilic and hydrophobic solid surfaces, we defined solid/liquid interface spacing as the distance between the surface and the peak value of the first water density layer. Near the gold surface, we found that interface spacing and peak value of first water density layer were constant and did not depend on bulk liquid pressure; near the silicon surface, those values depended directly upon bulk liquid. Our results reveal that the pressure dependence of Kapitza length strongly depends on the wettability of the solid surface. In the case of the hydrophilic gold surface, Kapitza length was stable despite increasing bulk liquid pressure, while it varied significantly at the hydrophobic silicon surface. © 2013 AIP Publishing LLC. [<http://dx.doi.org/10.1063/1.4851395>]

I. INTRODUCTION

Rapid progress in Micro and Nano Electro Mechanical Systems (MEMS and NEMS) has been challenged by the thermal transport problem in nanoscale.¹ The performance and reliability of these systems directly depend on the removal of latent heat by transporting either to the ambient surrounding environment or to a coolant system. In such cases, understanding the properties of thermal resistance at solid/liquid interfaces between nanoscale device components and surrounding/confined fluids, as well as between suspended nanoparticles and their fluid medium in nano-fluidics coolants, is critical to thermal management design.

The thermal resistance at a solid/liquid interface, known as the Kapitza resistance, was discovered by Kapitza in 1941.² One can also define the Kapitza length as the thickness of the bulk medium extrapolated from the temperature profile of liquid to solid where the wall temperature is reached.³ There are many experimental, theoretical, and computational studies regarding Kapitza length and its dependence on multiple molecular properties. For instance, the effect of vibrational mismatch between solid and liquid on interfacial thermal resistance has been characterized as a function of relative thermal oscillation frequencies, solid/liquid interaction strength, temperature gradient, wall temperature, and surface

topology.⁴⁻¹⁰ However, we are still far from a complete understanding. Further study is required to characterize the interfacial properties to enhance the heat dissipation efficiency.

As an alternative to experiments, computer simulations of several pioneers in the effect of fluid film confined between solid walls has been widely accepted. Thompson *et al.*¹¹ indicated that the confinement produces a marked shift in the bulk transition pressures of both spherical and chain molecules, and the shift depends on surface/fluid interaction strength. The strong surface/fluid interaction was also found as a main reason result the increase of density as the wall spacing was narrowed.^{12,13} Fluid adjacent to solid surface needs to be characterized since the structure and properties of interfacial liquid strongly affect the interfacial transport. In nano-confinements, surface forces result in the ordering of fluid molecules adjacent to the surface known as density layering. In this case, density structures formed on the surface depend on the surface/fluid interactions at the interface as well as the fluid properties in the bulk. For the latter, the bulk fluid pressure is expected to have a strong influence on the number of fluid molecules in contact with the solid surface. According to the acoustics mismatch theory, thermal boundary resistance is proportional to the acoustic impedance of $(\rho c)^{-1}$, where c and ρ are the phonon velocity and density of liquid, respectively. Hence, thermal resistance is expected to decrease as pressure increases. However, several authors have reported behaviors that contradict this theory. For

^{a)} Author to whom correspondence should be addressed. Electronic mail: bohunk@ulsan.ac.kr

example, Swartz *et al.*¹⁴ observed pressure dependence of thermal boundary resistance only at very low temperatures, concluding that thermal boundary resistance is usually independent of pressure. Despite the common use of water nano-confinements in numerous applications, there is still ambiguous understanding of the pressure dependence of thermal resistance at the solid/water interface.

The wetting behavior of a solid surface is another important factor that influences heat transfer at the solid/liquid interface.^{5–7} For instance, the transport of thermal energy measured using the time-domain thermo-reflectance method found the Kapitza length at hydrophobic surfaces to be 2–3 times greater than its length at hydrophilic surfaces.⁴ In such cases, the surface wetting behavior determines the surface/fluid structure and affects phonon coupling at its interface. Thus the surface/fluid structure at different bulk fluid pressures is expected to depend on wetting behavior.

Molecular dynamics simulations provide valuable insight into interface energy transfer mechanisms. Molecular dynamics considers the physical movements of molecules based on intermolecular interactions. The interaction parameters between pairs of identical molecules are obtained by empirical models, while the interaction parameters of non-identical molecules are estimated from parameters of the pair of identical molecules using mixing rules.¹⁵ Frequently, the solid/liquid interaction strength values are calculated as $\epsilon_{sl} = \sqrt{\epsilon_{ss}\epsilon_{ll}} = \alpha\epsilon_{ll}$ using solid/solid (ϵ_{ss}) and liquid/liquid (ϵ_{ll}) interaction strengths as well as a modulated coefficient (α). Previous researchers have reported α values ranging from 0.1 to 10,^{3,5–7,16–19} reflecting earlier attempts to simulate proper interface physics. However, the interaction parameters between identical molecules are optimized in a bulk material system and may need to be reparameterized for non-identical pairs instead of using simple mixing rules. One methodology is the measurement of the water contact angle to define the interactions between water and solids,^{20–22} which properly characterizes liquid/solid interactions and recovers wetting behavior.

The objective of this study was to investigate the pressure dependence of Kapitza length at the interface between water and solid surfaces with different wetting behaviors. To this end, we performed molecular dynamics simulations of water thin films confined between gold and silicon surfaces, which have been experimentally characterized as hydrophilic and hydrophobic, respectively. We utilized calibrated gold/water and silicon/water interaction parameters, which correctly reparameterized the wetting behaviors by capturing water contact angles of 25° for the gold surface²⁰ and 89° for the silicon surface.²¹ In order to further characterize the behavior of Kapitza length, we examined the water structure near the hydrophilic and hydrophobic surfaces at different bulk water pressures.

This paper is organized as follows: In Sec. II, we describe the molecular dynamics simulations of gold/water and silicon/water systems along with the interaction parameters used in this study. Section III describes the investigation of heat conduction in nano-channels and the determination of the Kapitza length at solid/liquid interfaces. Molecular dynamics simulations were used to calculate liquid water pressures at

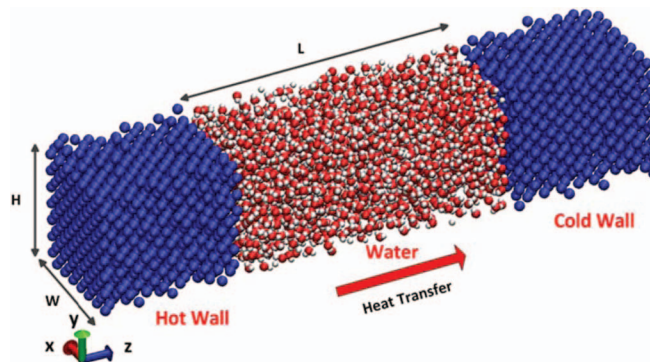


FIG. 1. Schematic of the simulation domain.

different densities, which were compared with existing thermodynamics values of the corresponding states. The structures of liquid water formed on hydrophilic and hydrophobic surfaces were examined at different bulk water densities. The interface coupling of water and hydrophilic/hydrophobic surfaces was characterized by defining the interface spacing between the nearest water density layer and the solid surface. Finally, we used the behavior of this interface spacing as a function of pressure to explain the pressure dependence of Kapitza length, and end with the conclusions from our study.

II. SIMULATION DETAILS

A schematic diagram of gold/water and silicon/water systems is shown in Figure 1. Each system was composed of two parallel solid walls with liquid water confined between them. Gold walls were constructed with face-centered cubic (FCC) structure consisting of two $7a \times 7a \times 8a$ unit cells with lattice constant $a = 4.08 \text{ \AA}$. Diamond structure of silicon lattice crystal walls consisted of $5a \times 5a \times 6a$ unit cells with $a = 5.43 \text{ \AA}$. The distances between the two walls were 69.074 \AA and 65.18 \AA in the z -direction for gold and silicon channels, respectively. The outermost layers of both sides of the simulation domains were fixed to their original positions to maintain constant volume systems. Thermostats were placed at the outermost second, third, and fourth layers of both solid walls, and the remaining atoms were free to move. That means thermostat reservoirs were small groups of solid atoms next to the outermost layers on the left and right hand side of the system corresponding to hot and cold regions, respectively. The remains of solid atoms and liquid water in the system were free to move without thermostat applied when heat transfer occurred. Periodic boundary conditions were enforced in x - and y -directions. The number of liquid water molecules was artificially adjusted to obtain different water pressures inside the nano-channels. Details of the system dimensions are shown in Table I.

Many different models for liquid water have been developed by fitting some physical properties of water; as a result, different models show agreement with the different properties of water. A model requiring more fitting parameters gives better results, but becomes computationally inefficient due to its complexity. On the other hand, many studies showed that the thermodynamic properties of water models were most sensitive to the van der Waals repulsive, short-range Coulomb,

TABLE I. Molecular parameters used for simulation domains.

Wall	Lattice structure	Lattice constant, a (Å)	Number of molecules in each layer	Number of layers in each wall	Lattice crystal wall	Liquid region length, L (Å)
Silicon	Diamond	5.43	50	25	5a × 5a × 6a	65.18
Gold	FCC	4.08	98	17	7a × 7a × 8a	69.074

and the polarization components of the potential.²³ Thus, the model explaining the van der Waals and Coulombic interactions with a proper polarization of water structure provides a fair understanding of complex water behavior.

Water models can be classified by the number of points used to define the model, and whether the structure is treated as rigid or flexible. In our study, for the purpose of simplicity and computational efficiency, we chose extended simple point charge (SPC/E) model which can be described as effective rigid pair potentials composed of Lennard-Jones (LJ) and Coulombic terms.²⁴ This water model has three interaction sites, corresponding to the three atoms of the water molecules. Each atom gets assigned a point charge to model the long-range Coulombic interactions, and the oxygen atom also exhibits LJ potential to model van der Waals forces. In particular, the partial charges $q_O = -0.8476e$ and $q_H = 0.4238e$ were assigned to oxygen and hydrogen atoms to model Coulombic interactions. Long-range electrostatic forces were calculated by a particle-particle, particle-mesh (PPPM) solver.¹⁵ The harmonic O–H bond length of 0.1 nm and the H–O–H angle of 109.47° were kept rigid using the SHAKE algorithm.²⁵ LJ interactions were calculated between the wall molecules and the oxygen atoms of the liquid water. We use the truncated LJ (12–6) potential to model the van der Waals interactions given as

$$V_{truncated}(r_{ij}) = 4\epsilon \left[\left(\left(\frac{\sigma}{r_{ij}} \right)^{12} - \left(\frac{\sigma}{r_{ij}} \right)^6 \right) - \left(\left(\frac{\sigma}{r_c} \right)^{12} - \left(\frac{\sigma}{r_c} \right)^6 \right) \right], \quad (1)$$

where ϵ is the binding potential between solid and liquid, r_{ij} is the intermolecular distance, σ is the molecular distance, and r_c is the cut-off distance. Conventionally, a cut-off distance of 1 nm is employed to simulate LJ potentials, which is approximately equal to 3σ .¹⁵ The forces applied on a particle i from all other particles within cut-off sphere were computed exactly, the particles did not feel any LJ pair interactions beyond the cut-off. However, accurate prediction of pressure was no longer valid, the thermodynamics state of liquid required considering of the long-range force field between the particles, while very large cut-off distance could magnify computational cost of MD simulations.²⁶ Therefore, an appropriate longer cut-off distance of 1.5 nm (approximately equal to 5σ) supplemented by tail correction term helped us validate the full theoretical LJ potential to the energy and pressure in efficient way.²⁷

Interatomic forces between the gold molecules were modeled by the embedded atom method (EAM),²⁸ which describes the total energy of a metal by calculating the embedding energy as a function of the atomic electron density. For silicon, we used the Stillinger-Weber model to describe two-body and three-body interactions and enforce the correct coordinate tetrahedral bonded structure.²⁹ The interactions of gold and silicon with water were calculated using the interaction strength and distance parameters of $\epsilon_{Au/O} = 0.02558$ eV, $\sigma_{Au/O} = 3.6$ Å and $\epsilon_{Si/O} = 0.01511$ eV, $\sigma_{Si/O} = 2.633$ Å, which produced the wetting contact angles of 25° and 89° on gold²⁰ and silicon²¹ surfaces, respectively. The calibration of interaction energy process reported as varying the interaction parameters between solid and liquid water in order to match the microscopic contact angle calculated by MD simulations with the experimentally measured macroscopic contact angle. Those water contact angle values induced by using the calibration interaction strength between solids with water above are consistency with the experimental contact angle values in report of Schrader *et al.*³⁰ and Martinez *et al.*,³¹ respectively. The details of molecular parameters used are given in Table II.

We divided the simulation systems into slab bins. Two different bin sizes of 0.067 nm and 0.2 nm were utilized to determine temperature, stress, and density distributions. The local temperature in each slab bin was calculated using the average atomic kinetic energies as $T = \frac{1}{3N_n k_B} \sum_{i=1}^{N_n} m_i V_i^2$, where k_B is the Boltzmann constant, N_n is the number of atoms in a slab bin, and m_i and V_i are mass and velocity of i th atom in the layer, respectively.

We calculated three orthogonal stresses normal to the x -, y -, and z -directions in the water domain (S_{xx} , S_{yy} , and S_{zz}). Computations of the atomistic stress tensor included two additive components: kinetic and virial terms. The kinetic term calculates the linear momentum resulting from particle velocities, while the virial term considers the internal contribution from short-range van der Waals forces, long-range Coulombic interactions, and the internal constraint forces of the bonds and angles of water molecules.^{26,32} In particular, the stress

TABLE II. Intermolecular interaction parameters used in simulations.

Interaction	σ (Å)	ϵ (eV)	q (e)
H–H	0	0	0.4238
O–O	3.166	0.006739	–0.8476
Au–O ²⁰	3.6	0.02558	0
Si–O ²¹	2.633	0.01511	0

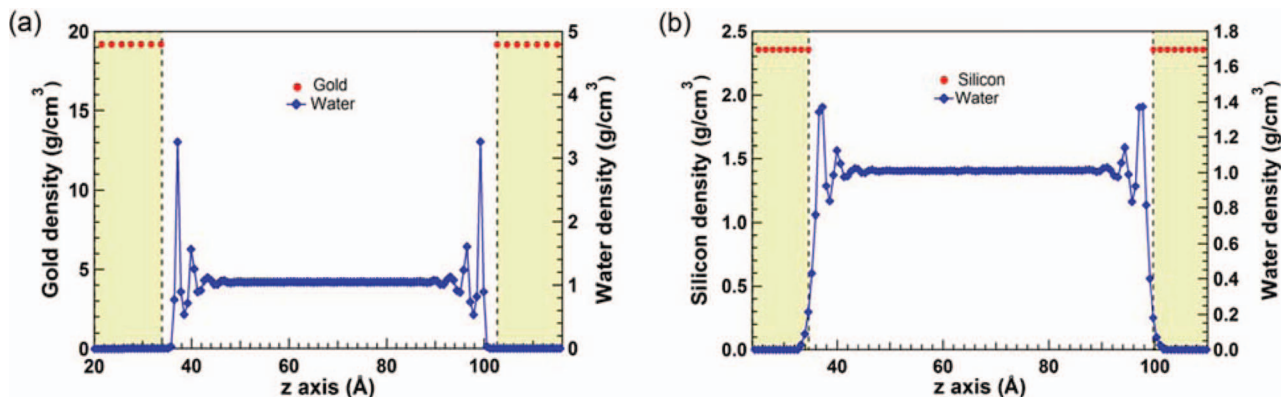


FIG. 2. Density profiles of liquid water confined in gold (a) and silicon (b) channels using 200-slab bins corresponding to a bin size of 0.067 nm. The surface temperature of left and right sides of each channel were set to 323 K and 283 K, respectively. The dashed line indicates the solid/liquid interface.

tensor for atom i is given by the following formula:³³

$$\begin{aligned}
 S_{\alpha\beta} = & - \left(m v_{\alpha} v_{\beta} + \frac{1}{2} \sum_{n=1}^{N_p} (r_{1\alpha} F_{1\beta} + r_{2\alpha} F_{2\beta}) \right. \\
 & + \frac{1}{2} \sum_{n=1}^{N_b} (r_{1\alpha} F_{1\beta} + r_{2\alpha} F_{2\beta}) \\
 & + \frac{1}{3} \sum_{n=1}^{N_a} (r_{1\alpha} F_{1\beta} + r_{2\alpha} F_{2\beta} + r_{3\alpha} F_{3\beta}) \\
 & \left. + Kspace(r_{i\alpha}, F_{i\beta}) + \sum_{n=1}^{N_f} r_{i\alpha} F_{i\beta} \right), \quad (2)
 \end{aligned}$$

where α and β are the Cartesian coordinates. The first term on the right hand side is the kinetic component where m is the atomic mass of particle i , v_{α} and v_{β} are the velocity components of particle i in the α and β directions. The second, third, fourth, and fifth terms are the virial components; the second term is a pairwise energy contribution where n loops over the N_p neighbors of atom i , r_1 and r_2 are the positions, and F_1 and F_2 are the forces of the two atoms in the pairwise interaction; the third and fourth terms are bond and angle contribution which atom i is part of; the $Kspace$ term is the contribution from long-range Coulombic interactions for PPPM solver; and finally, fifth term is the SHAKE internal constraint force to particle i . The per-atom array values above would be in product of stress and volume units. Therefore, the local stress tensor (S_{xx} , S_{yy} , and S_{zz}) in each slab bins was given as dividing the average of total per-atom stress tensor by the certain volume of slab bin.

Simulations began with NVT (constant number of molecules, constant volume, and constant temperature) ensemble to establish system equilibrium. In this state, the Maxwell–Boltzmann velocity distribution was used as the initial velocity for all molecules, and Nose–Hoover thermostat maintained system temperature of 300 K. In order to induce heat flux across the simulation domain, different temperatures were assigned to hot and cold reservoirs using Langevin thermostat, while the remaining solid lattices and fluid were maintained with NVE (constant number of molecules, con-

stant volume, and constant energy) ensemble. In this second state, heat transfer simulations were performed for 10 ns: 2 ns for the system to reach a steady state in the presence of applied heat, and two periods of 4 ns each in which temperature, density, and stress tensor distributions were measured. The simulation time step was set as 1.0 fs. All simulations were performed using LAMMPS.³⁴

III. RESULTS

A. Density, normal stress, and temperature profiles of liquid water within nano-channels

Density profiles of water confined in gold and silicon channels are given in Figures 2(a) and 2(b), respectively. Water density exhibits oscillatory behavior over several atomic distances from the solid surface. The water density oscillation gradually converges to the constant value of 1 g/cm³ in the bulk region of channel. This oscillation is observed since the molecules are ordered in the vicinity of the solid interface due to the dominance of surface forces. These forces were more extensive on the hydrophilic gold than the hydrophobic silicon surface, leading to higher peak water density near the gold surface. In addition to its strong attractive forces that create stronger oscillations, hydrophilic gold has profound repulsive forces that create a depletion layer immediately adjacent to its surface. The depletion layer is a zero-density region between liquids and solid surfaces that has been observed both experimentally³⁵ and mathematically.³⁶ In contrast, water penetrates into the first silicon layer as reported by Barisik *et al.*,²¹ creating no zero-density region. In particular, the solid silicon has lower atomic packing factor ($APF_{Si} = 0.34$) than the gold ($APF_{Au} = 0.74$).³⁷ This indicates that silicon crystal structure is less dense and has plenty of empty space.³⁸ Thus, water molecules can penetrate into the silicon lattice while densely packed gold structure does not allow such occurrence and even strong repelling forces create a depletion layer next to surface.^{38,39} Instead, we can define “solid/liquid interface spacing” as the distance between the solid surface and the peak value of the first water density layer. Solid/liquid interface spacing is less between water and silicon than between water and gold due to the weaker surface forces and less dense structure of silicon.

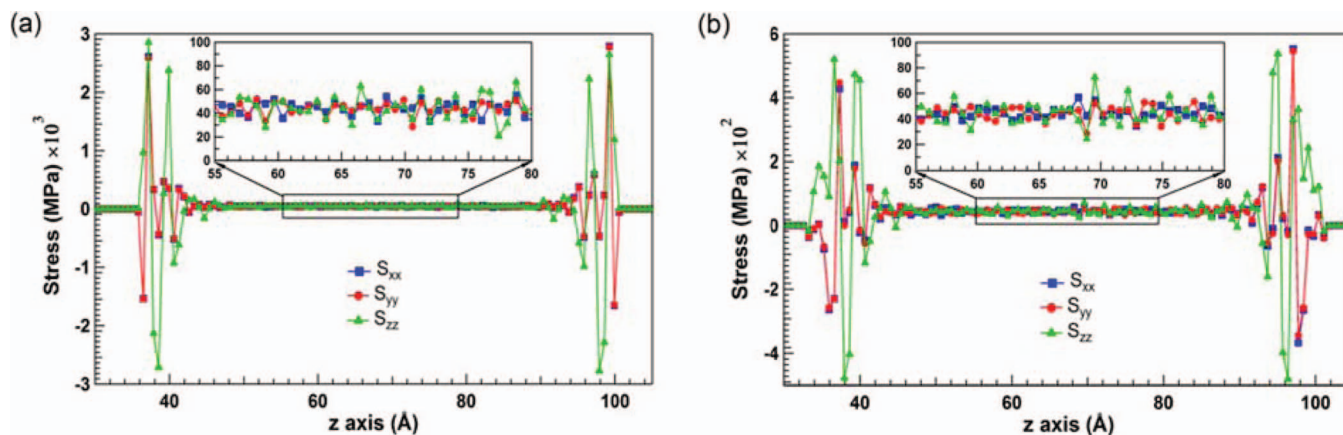


FIG. 3. Normal stress distribution of liquid water confined in gold (a) and silicon (b) channels using 200-slab bins. The surface temperature of left and right sides of each channel were set to 323 K and 283 K, respectively. Inset shows a close-up view of the normal stress distributions in the bulk region of the channels.

The normal stress distributions of liquid water in gold and silicon channels using 200 slab bins are plotted in Figures 3(a) and 3(b), respectively. Normal stress oscillates near the solid/liquid interface due to the local density variation of liquid water. In light of this, it is impossible to define pressure at the solid/liquid interface. However, away from these oscillations, normal stress becomes isotropic and pressure can be calculated as the average of the three orthogonal normal stress components: $P = \frac{S_{xx} + S_{yy} + S_{zz}}{3}$. Liquid water pressures inside the gold and silicon nano-channels calculated using molecular dynamics were found to be 43.78 and 44.47 MPa at the corresponding densities of 1.0116 and 1.0111 g/cm³ and average temperatures of 302.48 and 303.6 K, respectively. These values are approximately equal to the thermodynamics pressures of 36.74 and 36.47 MPa (see Table III) under the same density and temperature conditions, indicating the compressed state of liquid water in the nano-channels.

Temperature distributions along the gold/water and silicon/water systems obtained using 200- and 67-slab bins are shown in Figure 4. In both channels, the hot reservoir on the left was maintained at 323 K, while the right reservoir was maintained at 283 K. In the bulk liquid region, local temperature varied in a linear function with position. The tempera-

tures measured by the fine and coarse slab bins were very similar in this region, confirming a steady state in the presence of applied heat flux. Near the solid surfaces, the local temperature obtained using the fine bin size of 0.067 nm oscillated due to the density layering of water, while the coarse bin size of 0.2 nm resulted in a nearly linear profile with minor oscillations near the surface. As mentioned in Sec. II, the local temperature was calculated by averaging total atomic kinetic energies in each slab bin. The limited number of liquid particles observed in some local bins induces fluctuations in temperature as a function of density. The local temperature oscillates near solid interface due to the significant density layering in fine slab bins. On the other hand, the fluctuation diminished in the coarse slab bins, since a larger slab bin contains more particles participating to the average and reducing the fluctuation. Furthermore, strong layering in the vicinity of the hydrophilic gold surface induces more temperature fluctuations than near hydrophobic silicon. Inside the solid domains, linear temperature profiles are observed except temperature jumps between thermostat-applied and thermostat-free solid layers. These artificial temperature jumps develop due to the applied thermostat, which adjusts atomic velocities to maintain a set temperature.⁴⁰ Between solid and liquid domains, existence

TABLE III. Comparison of pressures calculated by molecular dynamics with thermodynamics state in nanoscale confinements.

Solid wall	Water density (g/cm ³)	Number of water molecules	r _c (nm)	Average temperature of water (K)	P _{MD} (MPa)	P _{Table} (MPa) ⁴²	Error (%)	Liquid water state
Au	1.0116	1838	1.5	302.48	43.78	36.74	19.16	Compressed liquid
Au	1.0399	1885	1.5	304.25	116.46	111.1	4.82	Compressed liquid
Au	1.0679	1932	1.5	304.07	195.42	188.4	3.72	Compressed liquid
Au	1.0956	1979	1.5	302.76	281.35	270.4	4.05	Compressed liquid
Au	1.1241	2027	1.5	303.64	384.24	372.7	3.09	Compressed liquid
Au	1.1504	2072	1.5	301.80	486.65	502	-3.05	Compressed liquid
Si	1.0111	1607	1.5	303.60	44.47	36.47	21.93	Compressed liquid
Si	1.0371	1648	1.5	302.54	107.02	101.9	5.02	Compressed liquid
Si	1.0585	1687	1.5	302.50	167.25	160.2	4.4	Compressed liquid
Si	1.0830	1728	1.5	301.68	236.07	230.3	2.5	Compressed liquid
Si	1.1057	1768	1.5	302.50	316.46	303.5	4.27	Compressed liquid

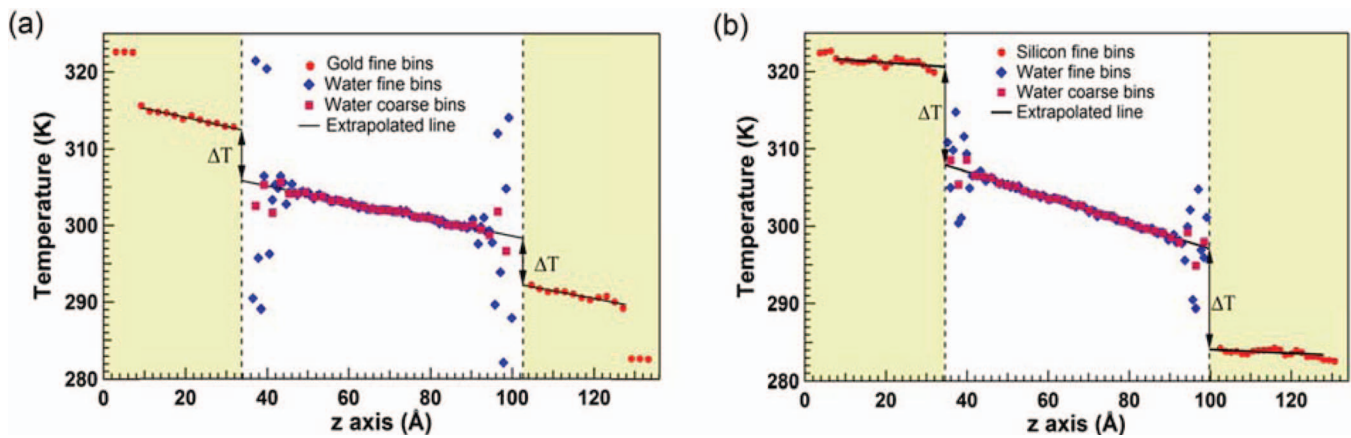


FIG. 4. Temperature profiles of liquid water confined in gold (a) and silicon (b) channels using 200- (fine) and 67- (coarse) slab bins corresponding to the bin sizes of 0.067 nm and 0.2 nm, respectively. The surface temperatures of left and right sides of each channel were set to 323 K and 283 K, respectively. The dashed line indicates the solid/liquid interface, and the solid black lines illustrate the linear least square fits of molecular dynamics results. Arrows indicate the temperature jump at solid/liquid interfaces.

of thermal resistance illustrated as a temperature jump at the interface, indicates a mismatch between the vibrational densities of solid and liquid phases.

B. Calculations of pressure, interface spacing, and Kapitza length

Figure 4 not only gives temperature distributions, but also illustrates the computation of the Kapitza length at solid/liquid interfaces. First, the local temperature gradient was calculated in the bulk regions of liquid domains. Second, a linear least-square fit through these points was extrapolated to the solid surface. Extrapolation of the local temperature from liquid regions onto the interfaces enabled us to define the temperature jump as the temperature difference between extrapolated liquid and solid temperatures. The temperature jumps at solid/liquid interfaces are indicated by arrows in Figures 4(a) and 4(b). Kapitza length is therefore given as a function of the temperature gradient of the liquid and the temperature jump at the interface as

$$\Delta T = L_K \left. \frac{\partial T}{\partial n} \right|_{\text{liquid}}, \quad (3)$$

where $\partial T/\partial n$ is the temperature gradient on the liquid side, and the temperature jump is $\Delta T = T_{\text{fluid}} - T_{\text{wall}}$. To elucidate the relationship between Kapitza length and liquid water pressure in nanoscale confinements, we performed a series of molecular dynamics simulations of thermal energy transport across solid/liquid interfaces by varying the number of liquid water molecules confined in the nano-channels.

In order to understand the effect of bulk water density on the near surface liquid structures, we studied the local density distributions by dividing the simulation domains into 800-slab bins. The density structures of water near gold and silicon surfaces with these finer slab bins are given in Figures 5(a) and 5(b). Similar to the observation illustrated in Figure 2, liquid density profiles exhibit pronounced oscillation near the solid surface. Despite the increase of bulk liquid density, the first density layers adjacent to the gold surface stayed unaffected,

as illustrated in Figure 5(a). The increase in bulk density did not change the density value and position of these layers. Therefore, the change of bulk water density inside the nano-channels did not affect the density structure formed on the hydrophilic gold surface. In addition, the pronounced density layering next to solid surfaces developed due to the surface forces forming solid-like ordering of water near surface. However, different than the solidified water density profile characterized by distinct peaks and significant empty space between them, observed liquid layering showed an oscillation region under the surface force effects and uniform density structure sufficiently away from surface in the center.⁴¹

In contrast, the water structure adjacent to the hydrophobic silicon surface was affected by bulk density. The density peak value of the first water density layers increased, and their locations deviated with increased liquid density in the bulk of the nano-channel as shown in Figure 5(b). We found that the increase in bulk liquid water not only enhanced the number of liquid molecules colliding with the silicon surface but also reduced their interface spacing. In addition, the existing penetration of liquid molecules into the silicon surface increased slightly under the effect of bulk liquid water. These findings suggest that variations in bulk density of a liquid confined in a hydrophobic silicon nano-channel play a critical role in the liquid structure at the solid surface.

In light of the observations at hydrophilic gold and hydrophobic silicon surfaces, we hypothesize that surface wettability significantly affects momentum exchange at the solid/liquid interface with different bulk liquid pressures by increasing the number of liquid molecules in contact with the surface. Figures 5(c) and 5(d) show variation in the S_{yy} components of normal stress with changes in liquid water density confined in gold and silicon channels, highlighting the correlation between pressure and bulk liquid density. Most likely the behavior of liquid water density distribution near solid surfaces, a dominant second stress peak and a much weaker third stress peak indicate the onset of the density layering effects on stresses tensor distributions. In the compressed state, small variations in liquid water density induce large deviations

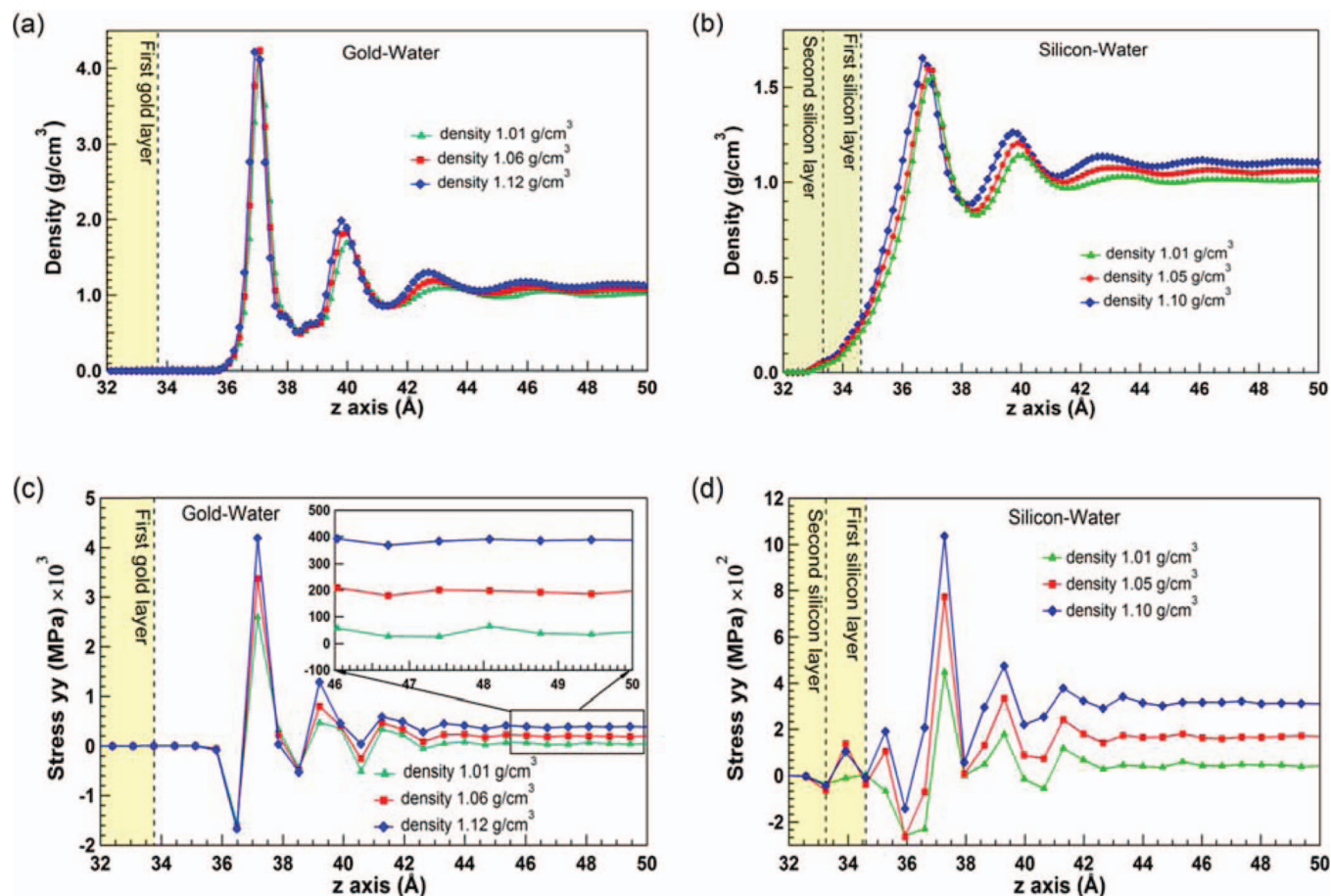


FIG. 5. Density distribution of water at different bulk liquid densities near gold (a) and silicon (b) channels using 800-slab bins corresponding to the bin size of 0.017 nm. Normal stress distribution in the y -direction of liquid water in gold (c) and silicon (d) channels. Inset shows a close-up view of the normal stress distribution in the bulk region of gold channel.

in pressure and in the resulting calculation of thermodynamic state, which is characteristic of nanoscale confinement systems (i.e., limited volume and finite number of molecules).

Figures 6(a) and 6(b) show the relationship between molecular dynamics-calculated pressures and thermodynamic state in both gold and silicon channels. As discussed with stresses tensor distributions in Figure 3, pressure was calculated by averaging the three orthogonal normal stress components in the bulk region, where all of them converged to a constant value. Molecular dynamics-calculated pressures showed a good agreement with the experimental values⁴² over a wide range of water densities (see Table III). Therefore, we concluded that liquid pressure predictions using the cut-off distance of 1.5 nm along with a tail correction term of long-range van der Waals interaction resulted in values comparable to existing thermodynamics pressures.

In order to validate the effect of bulk pressure on liquid water density near solid surfaces, we measured the solid/liquid interface spacing, defined as the distance between the solid surface and the peak value of the first water density layer. Figure 6(c) illustrates that the interface spacing does not depend on bulk liquid pressure, implying a relatively stable distance between the gold surface and the first water density layer. This means that the interface spacing is not compressible near the hydrophilic gold surface. In contrast, values as a

function of pressure in the silicon channel are plotted in Figure 6(d), in which the interface spacing decreased with increasing bulk liquid pressure, indicating the remarkable compressibility of the interface spacing near the hydrophobic silicon surface.

Kapitza length as a function of bulk liquid density in nanoscale confinements is plotted in Figures 7(a) and 7(b). Kapitza length, which reaches a constant mean value as shown in Figure 7(a), was not affected by bulk liquid water density in the gold channel. The convergence of Kapitza length can be explained by the strong adsorption of hydrophilic gold surfaces with liquid water molecules that results in a stable peak density value of liquid water despite increased bulk liquid density in the nano-channel. As a result, Kapitza length was independent of liquid pressures within the gold channel. This observation is consistent with the water structure obtained using 800-slabs bin in Figure 5(a), as well as the measurement in Figure 6(c) where the solid/liquid interface spacing is relatively stable despite increasing bulk liquid water density in the gold channel. In contrast, Kapitza length decreased linearly with increasing bulk liquid density near the hydrophobic silicon surface as shown in Figure 7(b). We found that the number of liquid water molecules in contact with the silicon surface increased with greater bulk liquid density in the silicon nano-channel, which in turn increased the

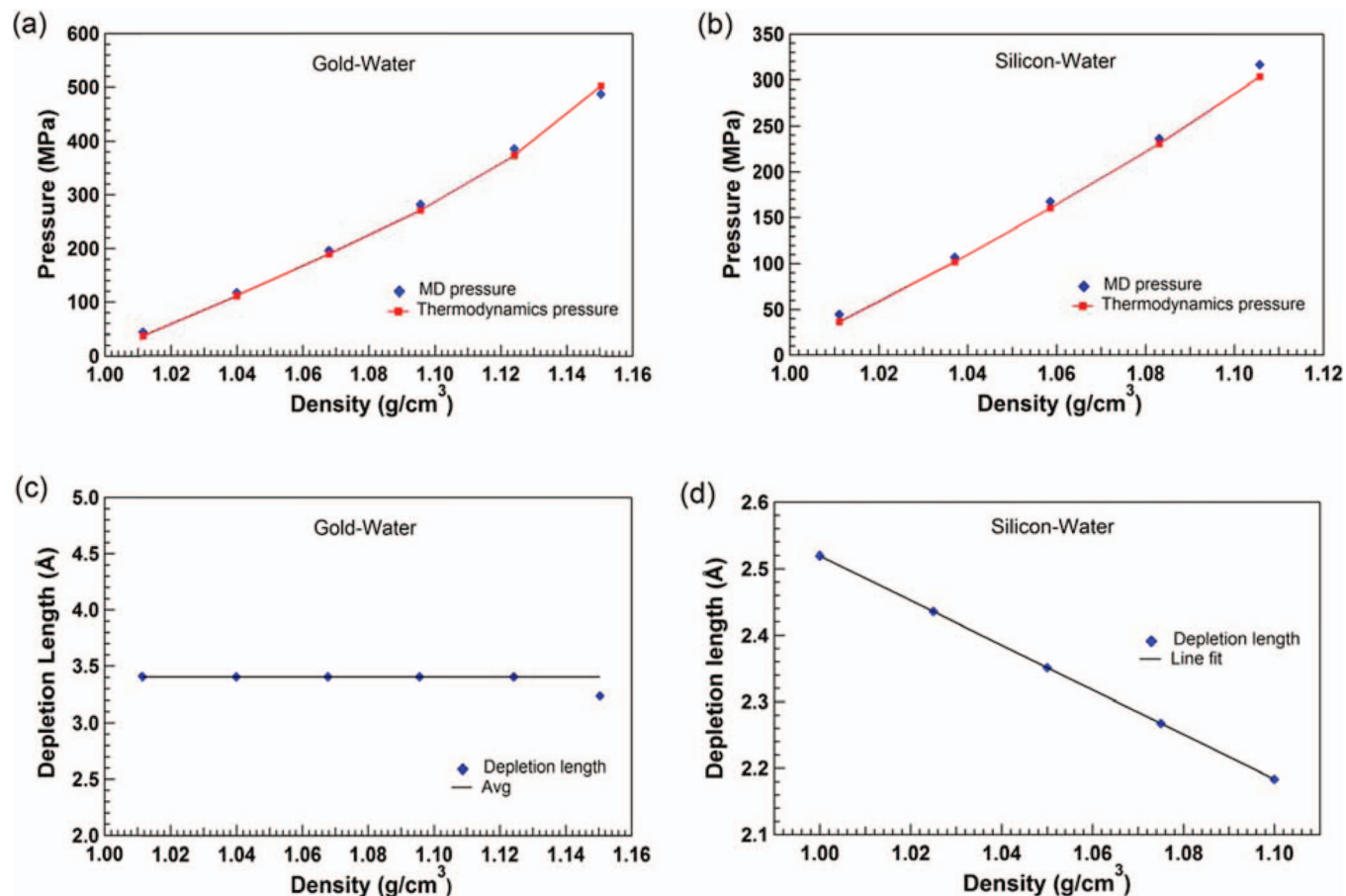


FIG. 6. Pressure versus density of liquid water confined in gold (a) and silicon (b) channels. Interface spacing between gold (c) and silicon (d) surfaces with the first liquid water density layer as a function of bulk liquid water.

probability of momentum exchange between silicon and water at the interface, thereby reducing Kapitza length. Kapitza length may also have been reduced by liquid water molecules penetrating the silicon walls and the compressibility of the interface spacing. Based on the results, we could imply a linear dependence of Kapitza length with the interface spacing at silicon surfaces. However, the interface spacing exhibited a quasi-universal relation with the surface wetting, surface roughness, surface temperature, and pressure effects.^{35,36}

Kapitza length also demonstrated complex dependence on various factors such as interaction strength, surface temperature, surface roughness, oscillation frequency of bi-materials at the interfaces. Therefore, a comprehensive correlation between the Kapitza length and the interface spacing needs further study.

We thus conclude that the wettability of solid surfaces is the key factor that determines the pressure dependence of Kapitza length at solid/liquid interfaces. The greater

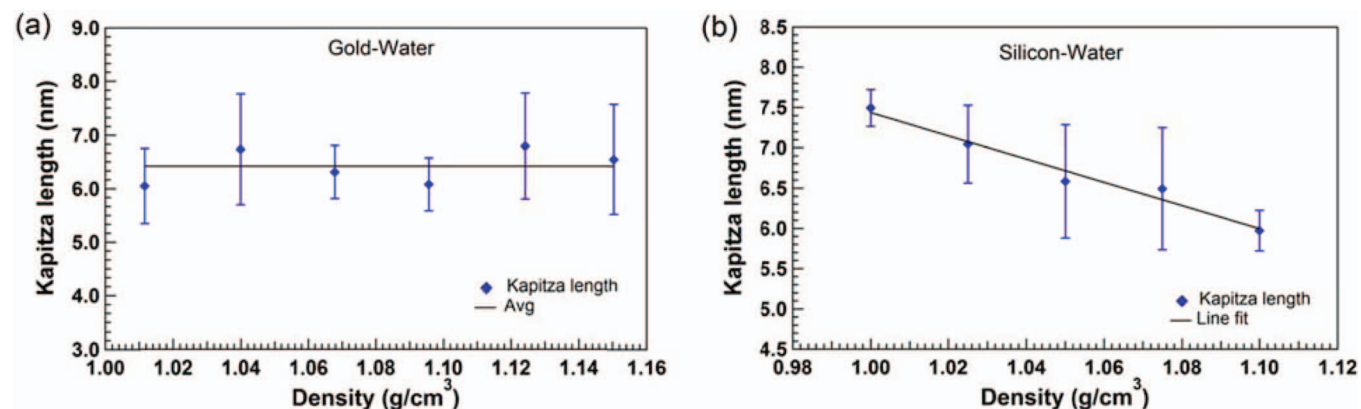


FIG. 7. Kapitza length at gold (a) and silicon (b) interfaces as a function of liquid water density. The error bars reflect the average of several independent simulations for determining Kapitza length at each density value. The solid lines indicate the characteristics of our results.

number of liquid molecules colliding with solid surfaces under the effects of bulk liquid pressure enhanced thermal energy transport across the solid/liquid interface, thereby reducing Kapitza length. For silicon, increase of pressure creates close packing between water and silicon molecules (smaller interface spacing) which develops a better coupling (more collisions between liquid and solid) enhancing the heat transport. The interpenetration of solid and liquid enhanced phonon transmission and reduced thermal resistance by providing additional phonon transport channels in the interfacial region.⁴³ Our results from the liquid water model differ from previously reported atomistic simulations of heat transfer based upon non-polar, monoatomic liquid molecules and their simple pairwise interaction potentials, which represented the negligible effect of liquid ordering adjacent to hydrophilic/hydrophobic solid surfaces on interface thermal transport.⁴⁴ Our results are consistent with the transport of thermal energy through solid/liquid interfaces as reported by Torii *et al.*,⁴⁵ as well as with the predictions reported by Xue *et al.*⁴⁴ involving the effects of complex liquid (water or chain-like molecular) layering on interface thermal resistance. Their model predicted that thermal energy transport through a solid/liquid interface is governed by the ordering of liquid structures in the vicinity of the solid surface.

IV. CONCLUSIONS

We have performed a systematic investigation of Kapitza length at solid/water interfaces under the effects of bulk liquid pressures using molecular dynamics simulations. We observed distinct behaviors of liquid water near hydrophilic gold and hydrophobic silicon surfaces. In gold channel, we measured a depletion zone immediately adjacent to the hydrophilic gold surface, with a constant magnitude of the first peak of liquid water density under changing bulk liquid water. In contrast, liquid water molecules penetrated into the hydrophobic silicon surface, and the first peak value of liquid density slightly increased with increasing bulk liquid water. Furthermore, temperature distributions along the nanochannels were obtained with temperature jump at solid/liquid interfaces, indicating the existence of interfacial thermal resistance.

We utilized a long cut-off distance reinforced by the long-range van der Waals tail correction term in order to calculate the normal stress components accurately. The pressure of liquid water confined in the nano-channels increased along with the bulk density of liquid molecules, and showed reasonable agreement with the thermodynamics state of liquid water by experimental data. Under the effects of bulk liquid pressures, the interface spacing was relatively stable near the hydrophilic gold surface, while it was highly sensitive to bulk liquid pressure in the silicon channel. In addition, the fluctuation of local pressures near the interface suggested the onset of the density layering effects on stresses tensor distributions. Under the compressed state, small variations in the liquid density of water caused large changes in pressure, providing unique behavior about the nature of materials arising from nanoscopic confinement.

Finally, our findings showed that Kapitza length was independent of liquid pressures in the hydrophilic gold channel. In contrast, Kapitza length decreased linearly with increasing bulk liquid density in the hydrophobic silicon channel. Based on the results, the pressure dependence of Kapitza length strongly depends on the wettability of the solid surface in which heat transfer is governed by the structure of liquid water in contact with the surface. The greater number of liquid molecules colliding with the surface enhances thermal energy transfer across the solid/liquid interface. In addition to the knowledge that Kapitza length depends on the boundary conditions of solid/water interaction strength as demonstrated by conventional molecular dynamics studies, the bulk liquid pressure dependence of Kapitza length directly depends on the wettability of solid surfaces. We are optimistic that our results will be applicable to nanochannel-confined liquids in future studies.

ACKNOWLEDGMENTS

This work was supported by the 2013 Research Fund of the University of Ulsan.

- ¹D. G. Cahill, W. K. Ford, K. E. Goodson, G. D. Mahan, A. Majumdar, H. J. Maris, R. Merlin, and S. R. Phillpot, *J. Appl. Phys.* **93**, 793 (2003).
- ²P. L. Kapitza, *J. Phys. (Moscow)* **4**, 181 (1941).
- ³J. L. Barrat and F. Chiaruttini, *Mol. Phys.* **101**, 1605 (2003).
- ⁴Z. Ge, D. G. Cahill, and P. V. Braun, *Phys. Rev. Lett.* **96**, 186101 (2006).
- ⁵B. H. Kim, A. Beskok, and T. Cagin, *J. Chem. Phys.* **129**, 174701 (2008).
- ⁶B. H. Kim, A. Beskok, and T. Cagin, *Microfluid. Nanofluid.* **5**, 551 (2008).
- ⁷B. H. Kim, A. Beskok, and T. Cagin, *Microfluid. Nanofluid.* **9**, 31 (2010).
- ⁸Z. Shi, M. Barisik, and A. Beskok, *Int. J. Therm. Sci.* **59**, 29 (2012).
- ⁹J. V. Goicochea, M. Hu, B. Michel, and D. Poulikakos, *J. Heat Transfer* **133**, 082401 (2011).
- ¹⁰H. Hu and Y. Sun, *J. Appl. Phys.* **112**, 053508 (2012).
- ¹¹P. A. Thompson, G. S. Grest, and M. O. Robbins, *Phys. Rev. Lett.* **68**, 3448 (1992).
- ¹²S. T. Cui, P. T. Cummings, and H. D. Cochran, *J. Chem. Phys.* **114**, 7189 (2001).
- ¹³A. Jabbarzadeh, P. Harrowell, and R. I. Tanner, *J. Chem. Phys.* **125**, 034703 (2006).
- ¹⁴E. T. Swartz and R. O. Pohl, *Rev. Mod. Phys.* **61**, 605 (1989).
- ¹⁵M. P. Allen and D. J. Tildesley, *Computer Simulation of Liquids* (Oxford University Press, 1989).
- ¹⁶J. Sun, W. Wang, and H. S. Wang, *J. Chem. Phys.* **138**, 234703 (2013).
- ¹⁷J. Sun, W. Wang, and H. S. Wang, *Phys. Rev. E* **87**, 023020 (2013).
- ¹⁸B. H. Kim, *Chem. Phys. Lett.* **554**, 77 (2012).
- ¹⁹G. Nagayama and P. Cheng, *Int. J. Heat Mass Transfer* **47**, 501 (2004).
- ²⁰S. Merabia, S. Shenogin, L. Joly, P. Keblinski, and J. L. Barrat, *Proc. Natl. Acad. Sci. U.S.A.* **106**, 15113 (2009).
- ²¹M. Barisik and A. Beskok, *Mol. Simul.* **39**, 700 (2013).
- ²²J. Rafiee, X. Mi, H. Gullapalli, A. V. Thomas, F. Yavari, Y. Shi, P. M. Ajayan, and N. A. Koratkar, *Nature Mater.* **11**, 217 (2012).
- ²³T. D. Jordanov, G. K. Schenter, and B. C. Garrett, *J. Phys. Chem. A* **110**, 762 (2006).
- ²⁴H. J. C. Berendsen, J. R. Grigera, and T. P. J. Straatsma, *J. Phys. Chem.* **91**, 6269 (1987).
- ²⁵J. P. Ryckaert, G. Ciccotti, and H. J. C. Berendsen, *J. Comp. Phys.* **23**, 327 (1977).
- ²⁶M. Barisik and A. Beskok, *Microfluid. Nanofluid.* **11**, 269 (2011).
- ²⁷M. Mecke, J. Winkelmann, and J. Fischer, *J. Chem. Phys.* **107**, 9264 (1997).
- ²⁸J. Mei, J. W. Davenport, and G. W. Fernando, *Phys. Rev. B* **43**, 4653 (1991).
- ²⁹F. H. Stillinger and T. A. Weber, *Phys. Rev. B* **31**, 5262 (1985).
- ³⁰M. E. Schrader, *J. Phys. Chem.* **74**, 2313 (1970).
- ³¹N. Martinez, "Wettability of silicon, silicon dioxide, and organosilicate glass," M.S. thesis (University of North Texas, 2009).
- ³²H. Heinz, W. Paul, and K. Binder, *Phys. Rev. E* **72**, 066704 (2005).

- ³³A. P. Thompson, S. J. Plimpton, and W. Mattson, *J. Chem. Phys.* **131**, 154107 (2009), see <http://lammps.sandia.gov> for more information.
- ³⁴S. J. Plimpton, *J. Comput. Phys.* **117**, 1 (1995).
- ³⁵M. Maccarini, R. Steitz, M. Himmelhaus, J. Fick, S. Tatur, M. Wolff, M. Grunze, J. Janecek, and R. R. Netz, *Langmuir* **23**, 598 (2007).
- ³⁶S. I. Mamatkulov, P. K. Khabibullaev, and R. R. Netz, *Langmuir* **20**, 4756 (2004).
- ³⁷W. D. Callister and D. G. Rethwisch, *Fundamentals of Materials Science and Engineering* (John Wiley & Sons, Inc., 2013).
- ³⁸T. M. Galea and P. Attard, *Langmuir* **20**, 3477 (2004).
- ³⁹R. S. Voronov, D. V. Papavassiliou, and L. L. Lee, *Ind. Eng. Chem. Res.* **47**, 2455 (2008).
- ⁴⁰M. Barisik and A. Beskok, *J. Comp. Phys.* **231**, 7881 (2012).
- ⁴¹L. Vrbka and P. Jungwirth, *J. Mol. Liq.* **134**, 64 (2007).
- ⁴²R. E. Sonntag and C. Borgnakke, *Table of Thermodynamics and Transport Properties: Computer-Aided Thermodynamics Tables Software Provided by Fundamentals of Thermodynamics* (Wiley, New York, 2002).
- ⁴³S. Shin, M. Kaviani, T. Desai, and R. Bonner, *Phys. Rev. B* **82**, 081302 (2010).
- ⁴⁴L. Xue, P. Keblinski, S. R. Phillpot, S. U.-S. Choi, and J. A. Eastman, *Int. J. Heat Mass Transfer* **47**, 4277 (2004).
- ⁴⁵D. Torii, T. Ohara, and K. Ishida, *J. Heat Transfer* **132**, 012402 (2010).